

# Large-area single-photon-counting CdTe detector for synchrotron radiation CT: a dedicated pre-processing procedure

LUCA BROMBAL,<sup>a,b\*</sup> SANDRO DONATO,<sup>a,b</sup> FRANCESCO BRUN,<sup>b</sup>  
 PASQUALE DELOGU,<sup>c,d</sup> VIVIANA FANTI,<sup>e,f</sup> PIERNICOLA OLIVA,<sup>g,f</sup> LUIGI RIGON,<sup>a,b</sup>  
 VITTORIO DI TRAPANI,<sup>c,b</sup> RENATA LONGO<sup>a,b</sup> AND BRUNO GOLOSIO<sup>e,f</sup>

<sup>a</sup>*Department of Physics, University of Trieste, 34127 Trieste, Italy,* <sup>b</sup>*INFN section of Trieste, 34127 Trieste, Italy,* <sup>c</sup>*Department of Physical sciences, Earth and Environment, University of Siena, 53100 Siena, Italy,* <sup>d</sup>*INFN section of Pisa, 34127 Pisa, Italy,* <sup>e</sup>*Department of Physics, University of Cagliari, 09042 Monserrato (CA), Italy,* <sup>f</sup>*INFN section of Cagliari, 09042 Monserrato (CA), Italy,* and <sup>g</sup>*Department of Chemistry and Pharmacy, University of Sassari, 07100 Sassari, Italy.*

*E-mail: luca.brombal@ts.infn.it*

## Abstract

Large-area CdTe single-photon-counting detectors are becoming more and more attractive in sight of low dose imaging applications due to their high efficiency, low intrinsic noise and absence of a scintillating screen which affects spatial resolution. At present, however, since the dimension of a single sensor is small (typically few cm<sup>2</sup>), multi-module architectures are needed to obtain a large field of view. This requires coping with inter-module gaps and with close-to-edge pixels, which generally show a non-optimal behavior. Moreover, high-Z detectors often show gain variations in time due

to charge trapping: this effect is detrimental especially in CT applications where a single tomographic image requires hundreds of projections continuously acquired in several seconds. This work has been carried out at the SYRMEP beamline of the Elettra Synchrotron Radiation facility (Trieste, Italy), in the framework of the SYRMA-3D project, which aims to perform the world's first breast-CT clinical study with synchrotron radiation. An ad-hoc data pre-processing procedure has been developed for the PIXIRAD-8 CdTe single-photon-counting detector, comprising an array of 8  $30.7 \times 24.8 \text{ mm}^2$  modules tiling a  $246 \times 25 \text{ mm}^2$  sensitive area, which covers the full synchrotron radiation beam. The procedure consists of 5 building blocks, namely dynamic flat fielding, gap seaming, dynamic ring removal, projection despeckling and around-gap equalization. Each block is discussed and compared, when existing, with conventional approaches. The effectiveness of the pre-processing is demonstrated for phase-contrast CT images of a human breast specimen. The dynamic nature of the proposed procedure, which provides corrections dependent upon the projection index, allows to effectively remove time-dependent artifacts, preserving the main image features including phase effects.

## 1. Introduction

In recent years high- $Z$  large-area single-photon-counting detectors have become appealing for imaging both in synchrotron and conventional sources experiments (Vedantham *et al.*, 2016). These detectors offer remarkable advantages over conventional indirect detection and charge integration systems. Properly operated high- $Z$  single-photon-counting detectors show minimum electronic noise (i.e., noise is Poisson dominated), energy discrimination of photons (i.e., spectral performances) and high detective efficiency (Ballabriga *et al.*, 2016; Takahashi & Watanabe, 2001). Moreover, unlike scintillator based detectors where an increase in the efficiency typically leads to a decrease

in the spatial resolution due to the scintillating process regardless of the pixel dimension, in direct conversion devices the spatial resolution is mainly limited by the pixel size (Taguchi & Iwanczyk, 2013). The aforementioned features make these detectors suitable for low dose phase-contrast imaging experiments, where both high efficiency for limiting the dose and high spatial resolution to detect phase-effects (e.g., edge enhancement) are needed.

At present, however, the data processing of large area high-Z single-photon-counting detectors is still challenging. In fact, given the limited area of a single sensor (typically few  $\text{cm}^2$ ) a large field of view is obtained via a multi-module architecture employing arrays or matrices of sensors (Delogu *et al.*, 2017b; Mozzanica *et al.*, 2016). These arrangements lead to the presence of non-negligible gaps between the sensors and require the use of the close-to-edge pixels which often show worse efficiency, stability and gain constancy. Furthermore, these detectors usually suffer from local charge-trapping effects that depends, in general, on the polarization time and on the exposure (Astromskas *et al.*, 2016; Park *et al.*, 2014; Pennicard & Graafsma, 2011; Knoll, 2010): these effects cause a gain variation in time which is detrimental especially in CT, where the scan duration may be in the order of several seconds or more (Delogu *et al.*, 2017a). In absence of a dedicated pre-processing procedure, all these effects cause artifacts which alter significantly the image quality, possibly impairing its scientific or diagnostic significance. In this work a pre-processing procedure tailored on the characteristics of a novel CdTe single photon counting detector (PIXIRAD-8 (Bellazzini *et al.*, 2013)) used for tomographic applications is presented. The implementation and optimization of the pre-processing are performed within the framework of the SYRMA-3D project, whose aim is to perform the world's first in-vivo synchrotron radiation breast-CT at the Elettra Synchrotron (Trieste, Italy) (Longo *et al.*, 2016; Sarno *et al.*, 2016; Longo, 2016; Delogu *et al.*, 2017b; Brombal *et al.*, 2018).

The beneficial effects of the pre-processing are shown directly on the reconstruction of a breast specimen which, due to the poor contrast given by adipose and glandular (or tumoral) tissues, represents a challenging sample. In the following, the procedure is described and the effects on the image reconstruction is reported step-by-step.

## 2. Material and Methods

### 2.1. Beamline, acquisition mode and sample

The images shown in this work were acquired at the SYRMEP (SYnchrotron Radiation for MEDical Physics) beamline at Elettra (Abrami *et al.*, 2005). The x-ray beam is produced by one storage ring bending magnet and monochromatized by means of a Si(111) double-crystal monochromator allowing to tune the energy in the range 8.5 keV - 38 keV, with a resolution of 0.1%. The beam cross section in the patient's room is 220 (horizontal)  $\times$  3 mm<sup>2</sup> (vertical, Gaussian shape, FWHM). The sample was imaged hanging from the patient support, composed of a rotating table with an ergonomically designed aperture at the rotation center. Thanks to the negligible divergence of the beam within the object (i.e., parallel beam geometry), the projections were collected only over 180 degrees, thus speeding up the acquisition. Each scan was performed in 40 seconds in continuous-rotation mode with an angular speed of 4.5 degrees/second (Delogu *et al.*, 2017b). The object-to-detector distance of 1.6 m (the maximum available in the present configuration) allows to detect phase effects and, along with the laminar shape of the beam, to work in a scatter-free geometry without the need of anti-scattering grids. The sample, fixed with formalin and sealed in a vacuum bag, was imaged at 32 keV delivering a mean glandular dose of 20 mGy. To calculate the dose, the air kerma at breast position is multiplied by a conversion factor accounting for breast size and glandularity, obtained from an ad-hoc developed Monte Carlo simulation based on a GEANT4 code optimized for breast dosimetry (Mettivier



*et al.*, 2015; Fedon *et al.*, 2015). The Directive 2004/23/EC of the European Parliament and of the Council of 31 March 2004 on setting standards of quality and safety for the donation, procurement, testing, processing, preservation, storage and distribution of human tissues were followed. The images reported in this study were acquired to guide the pathologist in the localization of lesions for the histological examination, according to the standard procedures of the Pathology Unit of the Academic Hospital of Cattinara, Trieste University, accredited by JCI (Joint Commission International). The sample was derived from surgical material sent to the Pathology Unit according to local guidelines for histological examination.

## 2.2. Detector

The detector used in this project is a large-area high-efficiency direct-conversion CdTe photon-counting device (PIXIRAD- 8) (Bellazzini *et al.*, 2013). It is made up by 8 modules and the pixels are arranged on a honeycomb matrix with 60  $\mu\text{m}$  pitch. Each block has a hybrid architecture in which the 650  $\mu\text{m}$  thick CdTe sensor and the readout electronics are coupled by means of the flip-chip bump-bonding technique. The active area of each block is  $30.7 \times 24.8 \text{ mm}^2$ , leading to a global active area of  $246 \times 25 \text{ mm}^2$ , corresponding to  $4096 \times 476$  pixels with a gap of 3 pixels between adjacent modules. Each pixel is associated with two independent 15-bit counters which can be used either in color mode (2 different energy thresholds, useful for chromatic imaging) or in dead-time-free mode. When the latter is selected, the detector fills one counter while reading the other, thus providing a zero-dead-time acquisition. The detector shows a linear response up to  $6.5 \times 10^7$  counts per  $\text{mm}^2$  per second (30 keV photons, 5 keV threshold) while its absorption efficiency is almost 100% for photon energy below 50 keV (Bellazzini *et al.*, 2013; Delogu *et al.*, 2016; Vincenzi *et al.*, 2015). The maximum photon flux used in this work corresponds to  $1.5 \times 10^7$  counts per  $\text{mm}^2$  per second,

while the threshold was fixed at 3 keV, which is sufficient to suppress the electronic noise. The projection images were collected at about 30 Hz (the maximum frame rate available) which, given the selected rotation speed, corresponds to 1200 projections per scan. Flat projections (i.e., without the sample) used for the flat fielding procedure were obtained prior to the scan with the same acquisition parameters. All the images are first streamed to the control PC via a Gigabit Ethernet connection and then they undergo the pre-processing procedure described in the next section.

### *2.3. Pre-processing*

The pre-processing procedure has a modular structure comprising 5 steps, specifically dynamic flat-fielding, gap seaming, dynamic ring removal, projection despeckling and around-gap equalization. All the steps will be described in the following sections. For the sake of portability and computational efficiency, the code is implemented in C language and it is made available upon request to the corresponding author. The complete pre-processing of 1200 16-bit raw projections, with a dimension of  $2300 \times 70$  pixels each, requires about 4 minutes on a 8 cores Intel Core i7-6700 CPU @ 3.40 GHz including loading and saving of the dataset.

*2.3.1. Dynamic flat fielding.* The flat fielding procedure is common to most of the x-ray imaging applications and it serves multiple purposes, namely to correct the beam shape and intensity inhomogeneity, to equalize the inhomogeneity in the pixel gain and to perform the normalization preparing the planar images to the CT reconstruction. The standard flat fielding consists of a pixel-by-pixel division of each projection image with a constant flat image (i.e., acquired without the sample). Defining  $P(x, y; t)$  as the projection image, with  $x, y$  the pixel coordinates and  $t$  the projection index proportional to the acquisition time, and  $\bar{F}_0(x, y)$  as the constant flat image, the

corrected image will be:

$$f_{\text{static}}(x, y; t) = \frac{P(x, y; t)}{\bar{F}_0(x, y)} . \quad (1)$$

Given a fixed detector's frame rate, the statistics of  $\bar{F}_0(x, y)$  is increased computing the average of  $(2w + 1)$  flat images, where  $w$  determines the width of the window:

$$\bar{F}_0(x, y) = \frac{1}{2w + 1} \sum_{t=1}^{2w+1} F(x, y; t) . \quad (2)$$

The choice of an odd number as the window width has been made for the sake of notation coherence: in the following most of the presented filter windows are centered in a pixel of interest so that an odd filter dimension is required. With this procedure, hereinafter referred to as static flat fielding, the presence of a detector's gain time-dependence in the projection images cannot be compensated since the flat image is not time dependent. On the contrary, the dynamic flat-fielding approach requires as many flat-field images as the number of projections so that the denominator of Eq. 1 can be substituted with a moving average of  $2w + 1$  flat images:

$$\bar{F}(x, y; t) = \frac{1}{2w + 1} \sum_{t'=t-w}^{t+w} F(x, y; t') , \quad (3)$$

in this way, assuming that the gain time dependence is reproducible, each flat image has both a high statistics and the same time dependence as the projection images.

The flat fielded projections will be:

$$f_{\text{dynamic}}(x, y; t) = \frac{P(x, y; t)}{\bar{F}(x, y; t)} . \quad (4)$$

In order for this approach to be used, a slow time dependence of gain is assumed so that, within the moving average window  $2w + 1$ , the flat images are considered to be constant. Namely, given a 30 Hz frame rate and a window  $2w + 1 = 11$  frames, the gain should not vary significantly for times of the order of 1 second. In addition, the fluctuations of the beam are assumed to be small in the time scale of the acquisition: this requirement is generally fulfilled at the Elettra synchrotron operated in top-up

mode, where 1 mA of ring current is injected every 20 minutes, having a baseline of 140 mA at 2.4 GeV. A different approach to the dynamic flat fielding based on principal component analysis can be found in (Van Nieuwenhove *et al.*, 2015).

*2.3.2. Gap seaming.* The PIXIRAD-8 detector, as most of the multi-module single-photon-counting devices, has a small gap (3 pixels wide) between each pair of modules which needs to be filled within the pre-processing procedure. The selected approach is a linear interpolation with a rectangular  $9 \times 8$  pixels kernel. For each pixel within the gap, the interpolation window is chosen to be half in the left module and half in the right one (regions *A* and *B* in Fig. 1), then the mean value of each half is computed and the gap-pixel value is defined as the weighted average of the two mean values:

$$f_{gap}(x, y; t) = \frac{u(x)}{N_A} \sum_{(x', y') \in A} f(x', y'; t) + \frac{v(x)}{N_B} \sum_{(x', y') \in B} f(x', y'; t) \quad (5)$$

where  $N_A = N_B$  is the normalization factor while the weights  $u(x)$  and  $v(x)$  are the normalized distances between the pixel within the gap and the regions *A* and *B*. Despite its simplicity, this procedure represents a good compromise between image quality and computational load. Nevertheless, more sophisticated approaches, such as the inpainting technique described in (Brun *et al.*, 2017), may be considered if wider gaps or high-contrast dishomogeneities in the sample are present.

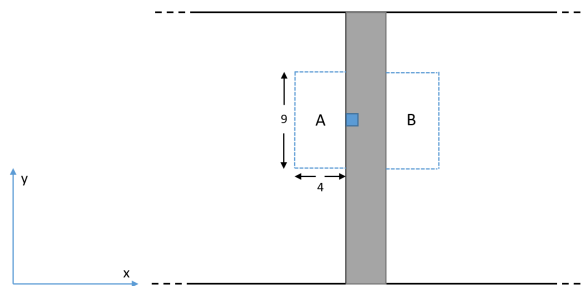


Fig. 1. illustration of the gaps seaming procedure. The gray region represents the gap while the rectangle is the interpolation window used for the pixel of interest (light blue). The figure is not to scale.

*2.3.3. Dynamic ring removal.* Ring artifacts, produced by gain inhomogeneities at the pixel level, are commonly encountered in tomographic reconstruction. In most of the cases the pixel (or group of pixels) producing the ring has a constant gain offset with respect to its neighbors, so that a single equalization is sufficient to remove or at least mitigate the artifact. In this case, despite the application of the dynamic flat fielding, some pixels still show a time dependent gain, resulting in rings with a non-constant intensity. To compensate for this artifact a dynamic ( i.e., depending on the projection index) equalization factor has to be used. The implemented ring-removal algorithm makes use of the alpha-trimmed filter, which is a hybrid of the mean and median filters. For each pixel, this filter takes a window of nearest neighbors, sorts their values, excludes the largest and the smallest values and replaces the pixel with the average of the remaining ones. Let  $g(i)$  be a one-dimensional image,  $h$  and  $c$  two integers that represent, respectively, the filter window and the confidence window half widths, with  $c < h$ . The alpha-trimmed filter algorithm can be described as follows.

- For each pixel  $i$ , consider the window of its  $2h + 1$  neighbors:

$$w(j) = g(i + j) , \quad -h \leq j \leq h \quad (6)$$

- Sort the values of  $w$  in ascending order:

$$w_s = \text{sort}(w) \quad (7)$$

- Substitute the pixel  $i$  with the average of  $w_s$  within the confidence window of size  $2c + 1$ :

$$\bar{g}_s(i) = \frac{1}{2c + 1} \sum_{j=-c}^c w_s(j) \quad (8)$$

Basically, in this average we are excluding the  $h - c$  smallest values and the  $h - c$  largest values. Note that if  $c = 0$  the alpha-trimmed filter reduces to the median filter, while if  $c = h$  it reduces to the mean filter. In a two-dimensional or three-dimensional image, the alpha-trimmed filter can be applied along each dimension: we will call  $S_x[g]$ ,  $S_y[g]$  and  $S_t[g]$  the images filtered along the dimensions  $x$ ,  $y$  and  $t$  respectively. Furthermore, we define the filter applied along two or three dimensions as the composition of two or three one-dimensional alpha-trimmed filters, as for instance  $S_{xy}[g] = S_x[S_y[g]]$ .

Given  $f(x, y, t)$ , the three-dimensional image describing the whole set of projections, and  $G_t^\sigma[f]$ , the convolution of the image  $f$  with a Gaussian function of standard deviation  $\sigma$  along the projection axis  $t$ , the ring removal algorithm consists of the following steps:

- First apply the alpha-trimmed filter to the projections along the dimension  $t$ , then filter them with a Gaussian convolution along the same dimension:

$$f_1(x, y, t) = G_t^\sigma[S_t[f]](x, y, t); \quad (9)$$

where  $\sigma$  should be a significant fraction of the number of projections.

- Apply the alpha-trimmed filter to  $f_1$  along the dimensions  $x$  and  $y$ :

$$f_2(x, y, t) = S_{xy}[f_1](x, y, t); \quad (10)$$

- $f_1$  is smooth along the dimension  $t$  by construction. It is also expected to be a smooth function along the dimensions  $x$  and  $y$ , therefore  $f_2$  and  $f_1$  should

be close to each other, unless there is an equalization problem. Evaluate the equalization correction factor as:

$$\alpha(x, y; t) = f_2(x, y; z)/f_1(x, y; t) \quad (11)$$

- Apply the correction factor to obtain the ring-corrected image:

$$f_{rc}(x, y; t) = \alpha(x, y; t)f(x, y; t) \quad (12)$$

In our implementation, we are using  $h_x = h_y = h_z = 10$ ,  $c = h/2$  for all dimensions and  $\sigma = N_p/10$ . Here we remark that the main advantage of this algorithm is that the equalization factor  $\alpha$  varies with the projection index, allowing to cope with non-constant ring artifacts. The results of this approach will be compared with two of the most known filters which tackle the ring-removal problem from different perspectives, namely the one proposed by Rivers (Rivers, 1998; Boin & Haibel, 2006), based on a moving average filtering, and the one proposed by Münch, based on a combined wavelet-Fourier filtering (Münch *et al.*, 2009).

*2.3.4. Projection despeckling.* In each projection image few (about 0.5%) pixels with an abnormal number of counts, either lower or higher than the neighboring pixels, are present. Their appearance is not reproducible neither in space nor in time and their content cannot be correlated with the actual number of impinging photons. To remove these speckles, which cause streaking artifacts in the reconstructed image, they first need to be recognized and then replaced. The procedure is based on a slightly different version of the alpha-trimmed filter described in the previous section, modified in order to filter only the bad pixels: for each pixel position  $i$  the average  $\bar{f}(i)$  and standard deviation  $\sigma(i)$  of the pixels comprised within a confidence window are computed, then the pixel of interest is replaced only if its value differs from the mean value more than  $N\sigma(i)$ ,  $N$  being a parameter of the filter. In this way  $N$  acts

as a filter sensitivity threshold, where if  $N \rightarrow 0$  all the pixels will be filtered, as in the implementation reported in Sec. , while if  $N \rightarrow \infty$  no pixels will be modified. Moreover, when calculating the average and standard deviation we are excluding the  $h - c$  smallest values and the  $h - c$  largest values, meaning that pixels with either abnormally high or low counts can be easily discarded. For the projection despeckling, the filter window is a  $5 \times 5$  pixels square and the confidence window is  $3 \times 3$  pixels square, while the optimization of the parameter  $N$  is reported in the results section.

*2.3.5. Around-gap equalization.* The last step of the pre-processing is a dedicated procedure for equalizing the pixels around the gaps between modules. This further equalization is required since several adjacent columns of close-to-edge pixels show a non-optimal gain behaviour. This effect involves a large number of pixel columns (30-40 columns across the gap), hence the action of the ring removal filter, which operates with a 10 pixels window, is not sufficient. This procedure is based on a moving average along the projection axis and it is described as follows.

- Given a projection  $t$ , a volume  $C$  of width  $2c = 40$  pixels, height equal to the full height of the projection and depth  $N_p/3$ , where  $N_p$  is the number of projection, is selected across the gap between 2 modules. Other two volumes ( $A$  and  $B$ ) with the same height, depth and a width of  $2a = 10$  pixels are selected adjacent to  $C$  (see Fig. 2).
- The mean value along  $x$  and  $t$  axis is computed for the volumes  $A$  and  $B$ :

$$\begin{aligned} \bar{f}_A(y; t) &= \frac{1}{2aN_p/3} \sum_{x=x_A-a}^{x_A+a} \sum_{t'=t-N_p/6}^{t+N_p/6} f(x, y; t') , \\ \bar{f}_B(y; t) &= \frac{1}{2bN_p/3} \sum_{x=x_B-b}^{x_B+b} \sum_{t'=t-N_p/6}^{t+N_p/6} f(x, y; t') . \end{aligned} \tag{13}$$



- The mean value along  $t$  is computed for the volume  $C$ :

$$\bar{f}_C(x, y; t) = \frac{1}{N_p/3} \sum_{t'=t-N_p/6}^{t+N_p/6} f(x, y; t') . \quad (14)$$

- The equalization factor is computed as:

$$Eq(x, y; t) = \frac{u(x)\bar{f}_A(y; t) + v(x)\bar{f}_B(y; t)}{\bar{f}_C(x, y; t)} . \quad (15)$$

where  $u(x)$  and  $v(x)$  are defined as in Sec.2.3.2.

- The image is multiplied for the equalization factor:

$$f_{around}(x, y; t) = f(x, y; t)Eq(x, y; t) . \quad (16)$$

In order for this procedure to be effectively used, the pixels within the regions  $A$  and  $B$  must not show a non-optimal behavior. Moreover, as mentioned for the dynamic flat fielding and ring removal steps, the around-gap fixing equalization factor depends on the projection index, thus allowing to compensate for slow gain variations of close-to-gap pixels.

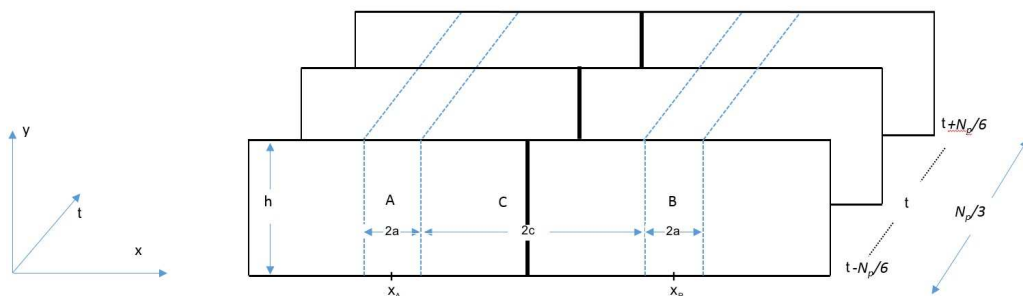


Fig. 2. Illustration of the equalization procedure: pixels of the projection  $t$  within the volume  $C$  are those to be equalized. See text for the complete description. The figure is not to scale.

#### 2.4. Image reconstruction

Prior to the tomographic reconstruction, the pre-processed projections can be optionally phase-retrieved. The benefit of a proper application of the phase retrieval algorithm, based on the homogeneous transport of intensity equation approach (Paganin

*et al.*, 2002), is to increase contrast-to-noise ratio while preserving spatial resolution, thus enhancing the visibility of low-contrast structures (Beltran *et al.*, 2011). The projections, either with or without the phase retrieval, are reconstructed via a GPU-based filter back projection (FBP) with a standard Shepp-Logan filtering. The reconstruction process, comprising the phase retrieval, requires less than 1 minute using a Nvidia GeForce GTX 1080.

### 3. Results and Discussion

In order to compare the flat fielding procedures in the projection space, two sets of 1300 flat projections were acquired with different photon fluences: one is collected with a low photon fluence to simulate the sample's absorption, the other, acquired with a 4 times higher statistics, is used for the flat fielding. This choice is made to uncouple the effects of time and exposure on the detector's gain, thus having two datasets with the same acquisition time (i.e., acquired after the same time from the polarization of the CdTe sensor) but different exposures. In Figs. 3 (a)-(b) a detail of the first projection normalized with the static and the dynamic flat field approach is reported: at the center of both images a cluster of pixels with a gain lower than the neighboring ones is present. Observing the same region at a later time, it is evident that the cluster exhibits a gain variation which is more pronounced for the static flat fielding, in Fig. 3 (c), with respect to the dynamic flat fielding, in Fig. 3 (d). Focusing on the intensity plots as a function time in Figs. 3 (e)-(f) of a group of pixels within the cluster, it is clear that the gain variation of the statically flat fielded ( $\sim 55\%$ ) dataset is significantly higher with respect to the one ( $\sim 20\%$ ) of the dynamically flat fielded projections. Moreover, as it should be expected, the latter shows a smoother time-dependence which can be better compensated by the ring-removal procedure. The effects of each uncompensated crystal defect can be traced through the tomographic

reconstruction process. In Fig. 4 (a) a detail of the reconstructed image corresponding to a row through the defective pixel cluster obtained with the static flat fielding is shown: a bright streak-like artifact embedded within a partial ring artifact, due to the uncompensated gain variation, is observed. Fig. 4 (b) reports the same detail when the dynamic flat field approach is used: in this case the streak is barely visible while the ring has been removed. In both images the whole pre-processing procedure has been applied in order to evidence only the effect of the flat fielding in the final reconstruction.

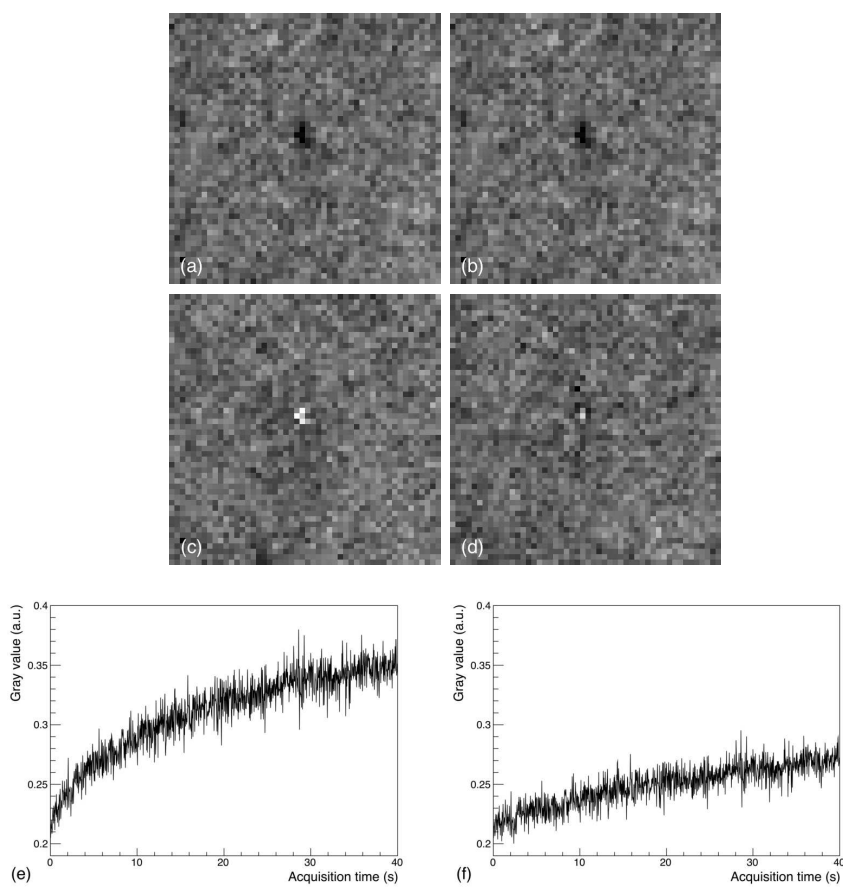


Fig. 3. Comparison between static and dynamic flat-fielding procedures in the projection space using two flat dataset with different statistics. In (a) and (c) the first and last projections when the static flat field is applied, in (b) and (d) the first and last projections when the dynamic flat field is applied. In (e) and (f) the average intensity of the bad pixel cluster as a function of time for the static and dynamic flat field respectively.

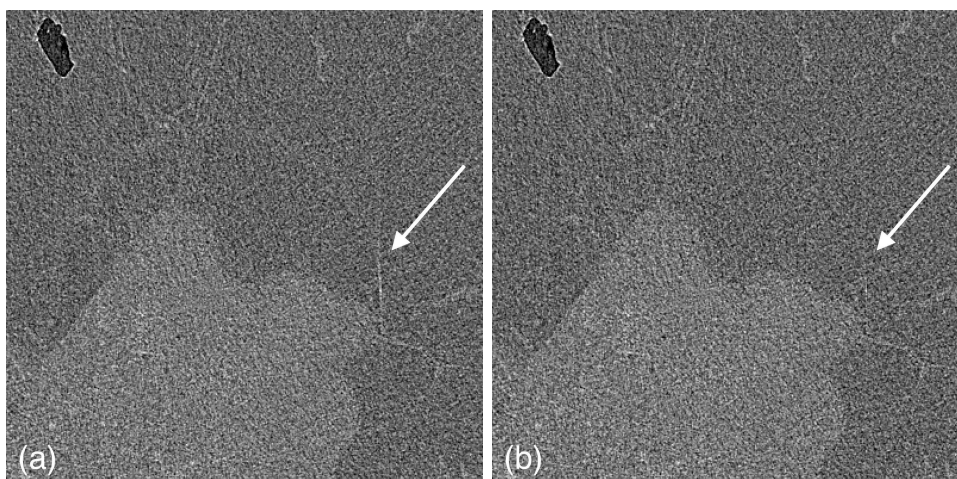


Fig. 4. Detail of a reconstruction obtained applying the static (a) and the dynamic (b) flat fielding. The arrow indicates a streak artifact clearly visible in (a) while it is barely visible in (b).

Figs. 5 (a)-(c) show, respectively, the sinogram and the tomographic reconstruction of the sample where only the flat fielding has been applied. The sample was imaged using 4 modules of the detector, thus in the sinogram only 3 gaps are visible, producing marked ring artifacts in the reconstruction. The artifacts cover only half of circumference because the projections are acquired over 180 degrees. In Figs. 5 (b)-(d) both the sinogram and the reconstruction are reported after the gap seaming: given the small size of the gaps (3 pixels wide) the interpolation does not introduce significant artifacts, thus preserving the anatomical information. Nevertheless, the resulting image is still affected from the presence of several artifacts which need to be corrected.

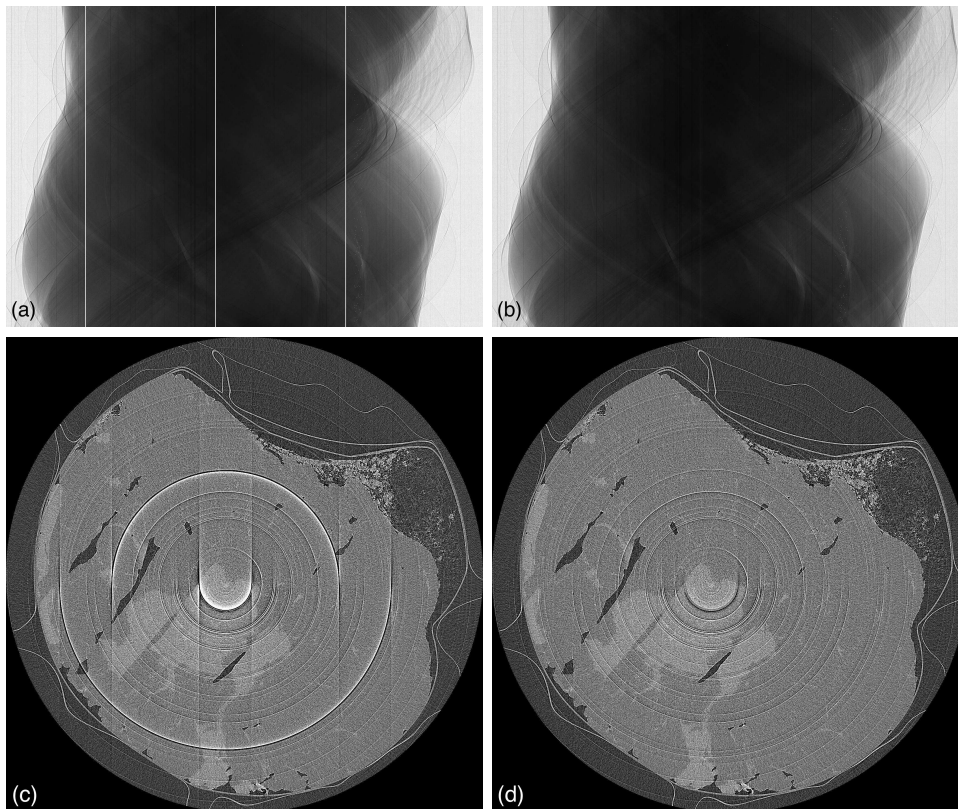


Fig. 5. Sinograms and reconstructions obtained before (a)-(c) and after (b)-(d) the gap seaming.

Figs. 6 (a)-(d) show the sinogram and the reconstruction where the Rivers ring-removal filter (Rivers, 1998; Boin & Haibel, 2006) has been applied with a window width of 11 pixels, while in Figs. 6 (b)-(e) the Münch filter (Münch *et al.*, 2009) has been applied with a decomposition level 5 and a width of the Gaussian band-pass function of 3. From the sinograms, it can be seen that neither the Rivers nor the Münch filter are optimal: in both cases most of the rings are only partially compensated resulting in arc (i.e., partial ring) artifacts. In particular, focusing on the Rivers approach where a constant equalization factor is used, the artifacts appear to be brighter in the top of the sinogram, well corrected in the central part and darker in the bottom. Again, this is due to the time gain variation which occurs to some pixels as previously described, e.g., plot of Fig. 3 (f). The Münch filter yields slightly bet-

ter results on the rings but it introduces a low spatial frequency modulation strongly affecting the image quality. Comparing these results with Figs. 6 (c)-(f), obtained with the procedure described in Sec. 2.3.4, it is clear that the latter yields the best results, substantially removing most of the ring artifacts. It is worth noticing that the main advantage of this approach is the presence of an equalization factor varying with the projection index.

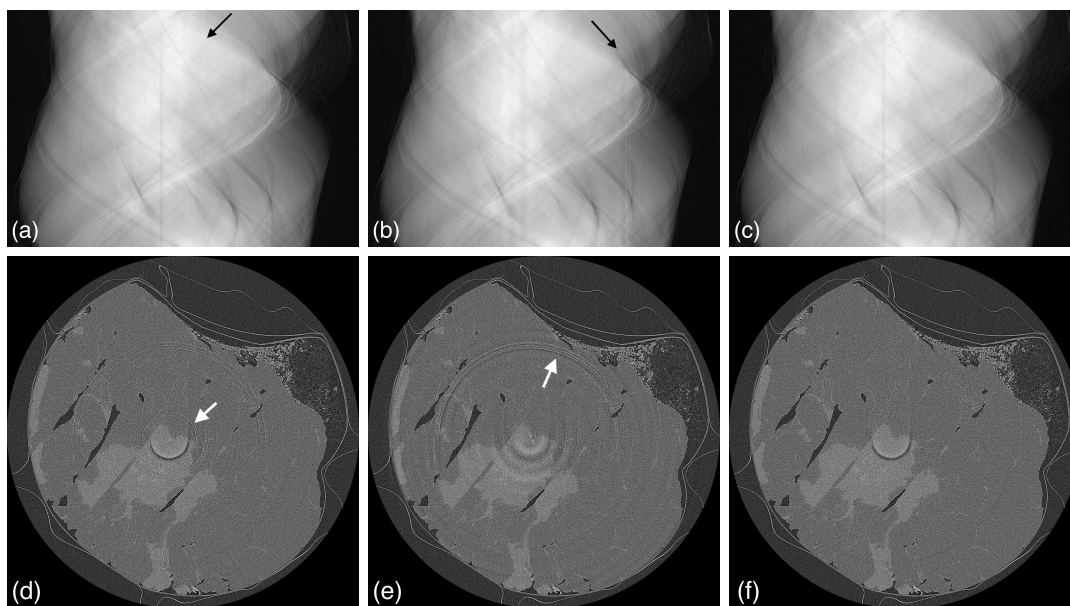


Fig. 6. Sinograms and reconstructions obtained applying the Rivers (a)-(d), Münch (b)-(e) and the dynamic (c)-(f) ring removal filters. Sinograms are inverted and displayed on a logarithmic scale for better visualizing the action of the filters. The arrows in both the sinograms and the reconstructions indicate uncompensated ring artifacts.

As reported in Sec. 2.3.4, the parameter  $N$  of the despeckling filter should be optimized in order to remove only the bad pixels. For this purpose a dataset of 1300 flat projections has been acquired and subdivided into two datasets consisting of the even and the odd projection respectively. Then the even projections were divided, pixel by pixel, by the odd projections. Thus, the gain dependence from time and exposure is matched and the distribution of the bad pixels alone can be studied. The gray

level histogram of the dataset obtained with this approach is plotted in Fig. 7 (a) (black dashed line): if no bad pixels are present, the distribution should be a gaussian centered around one, whose width is only dependent on the photon statistics. On the contrary, the presence of bad pixels widens the distribution on both sides. The despeckling filter is expected to suppress the tails of the distribution without affecting the width of the gaussian, i.e., the statistical noise. By varying continuously the filter parameter  $N$  it is found out that values around 15 satisfy this request (blue solid line) while, for lower  $N$  (e.g.,  $N=3$ , red dashed line), the statistical noise is reduced, thus the image is smoothed. The same overcorrection effect is observed when applying common despeckling filter, such as the median filter, as reported in Fig. 7 (b).

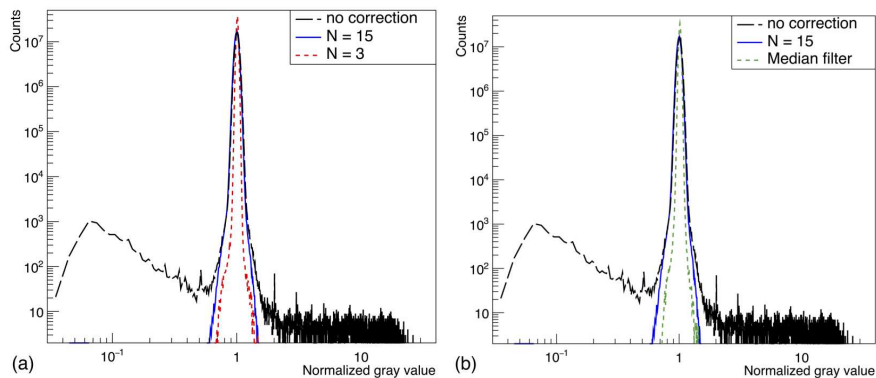


Fig. 7. Histograms for the despeckling filter optimization. In (a) the non filtered spectrum (black dashed line) is compared with the filtered ones (blue solid line for  $N=15$ , red dashed line for  $N=3$ ), in (b) also the median filtered spectrum (green dashed line) is reported.

Once the parameter  $N$  has been optimized, the despeckling filter can be applied to the projections. Figs. 8 (a)-(b) show a detail of the sinogram before and after the application of the filter respectively: the bad pixels have been removed without affecting the image noise and texture. The effect of the filter on the reconstruction is reported in Figs. 8 (c)-(d), where in the unfiltered image several striking artifacts due to bad pixels are visible. Here, it has to be remarked that the optimization of the



parameter  $N$  is crucial since an excessive smoothing of the projections may disrupt the edge-enhancement effect, which is one of the key features of the synchrotron radiation breast-CT.

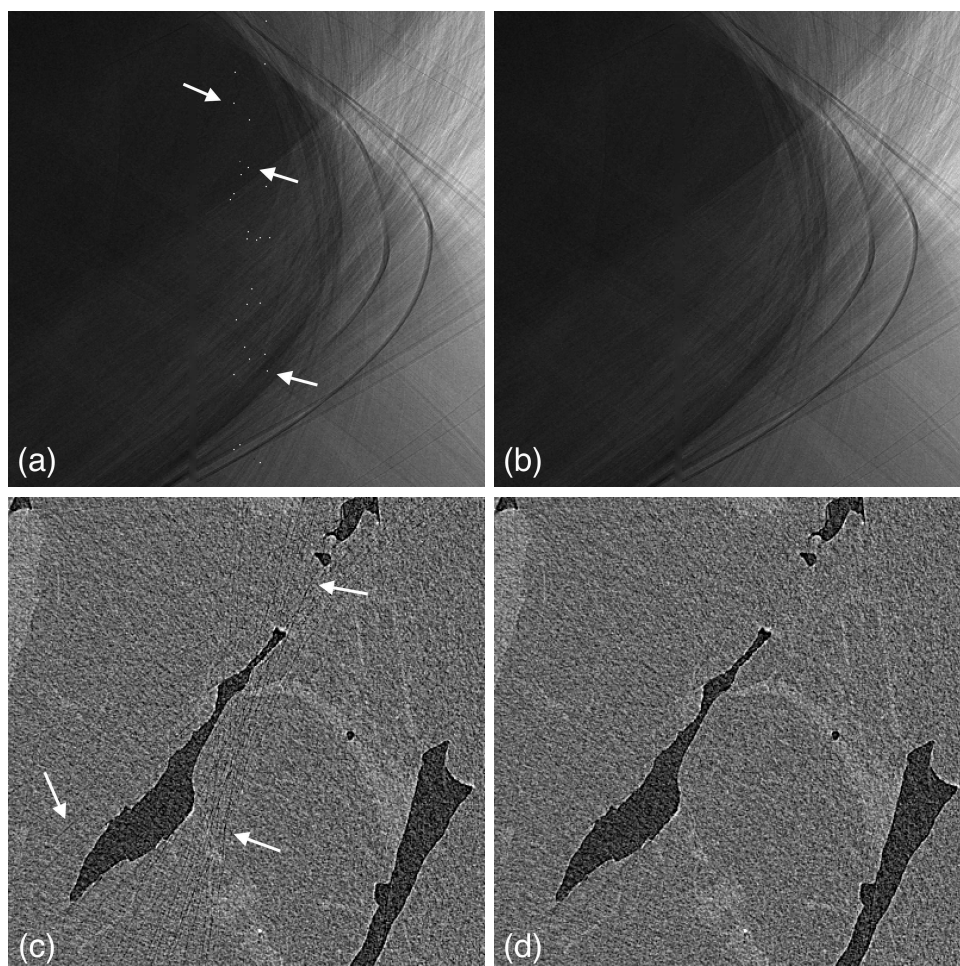


Fig. 8. Sinograms and reconstructions before (a)-(c) and after (b)-(d) and the application of the despeckling filter. The arrows indicate some of the speckles in the sinogram and some of the streaks in the reconstruction.

The last step of the pre-processing procedure is the around-gap equalization. In fact, referring to Fig 9 (a), two ring artifacts correspondent to the regions around the gaps between modules, can still be observed. Once the equalization procedure is applied the rings are removed and the final reconstructed image, reported in Fig 9 (b), is free from major artifacts.

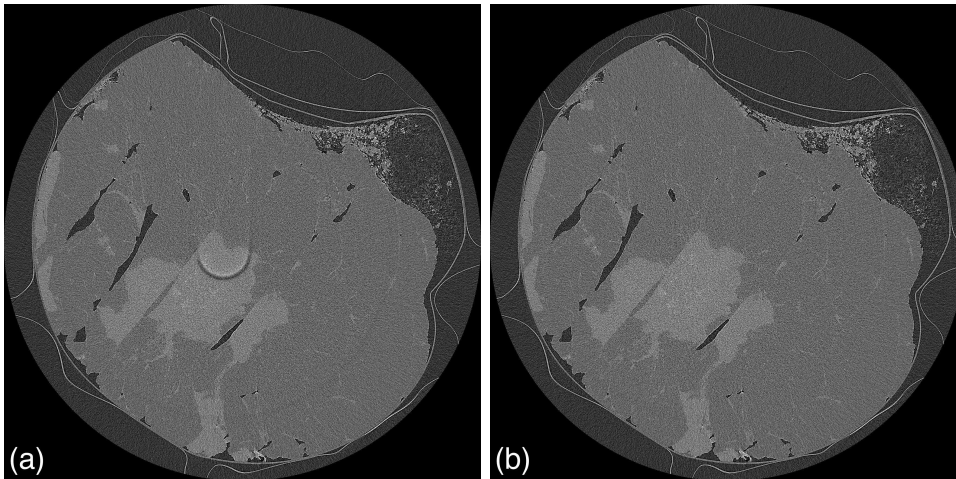


Fig. 9. Reconstructions before (a) and after (b) the around-gap equalization.

After the projections have been pre-processed, the phase-retrieval algorithm is applied (two materials approach,  $\delta/\beta = 869$  (Burvall *et al.*, 2011; Brombal *et al.*, 2018)). Noticeably, the phase-retrieval algorithms produces a remarkable increase in the contrast to noise ratio, thus highlighting also uncompensated artifacts which may be barely visible in the phase-contrast images. In Figs. 10 (a)-(b) a detail of the reconstruction processed only with the first two steps of the pre-processing procedure (namely, flat fielding and gap seaming) is reported, with and without phase retrieval: in both cases severe ring artifacts are observed but, when phase retrieval is applied, streaking artifacts arising from uncompensated speckles become evident, definitely impairing the image quality. Conversely, when the whole pre-processing is applied, both the absorption and phase-retrieved images in Figs. 10 (c)-(d) does not report significant artifacts. In this context, it should be stressed that the optimization of the pre-processing procedure must account also for the subsequent image processing (e.g., phase retrieval) in order to yield a high image quality. In Fig. 11 the final result of the data processing, comprising the pre-processing and the phase-retrieval procedure, is shown: the extension, shape and boundaries of both the tumoral and glandular tissue

(light gray) are clearly visible without artifacts.

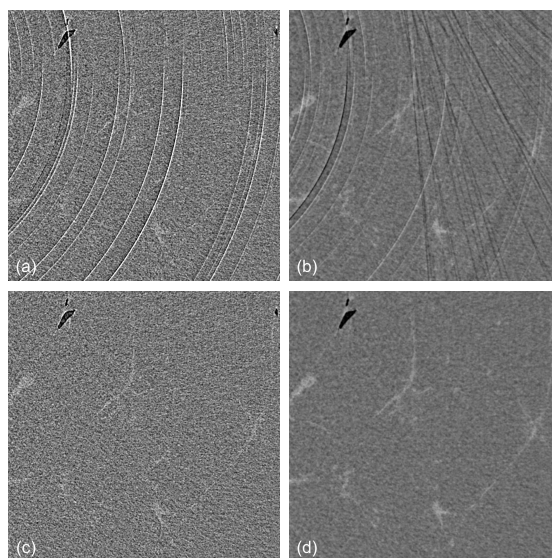


Fig. 10. Detail of a reconstruction without (a)-(c) and with (b)-(d) the phase retrieval. In (a)-(b) only the flat fielding and gap seaming steps are applied, in (c)-(d) the whole pre-processing procedure is used.

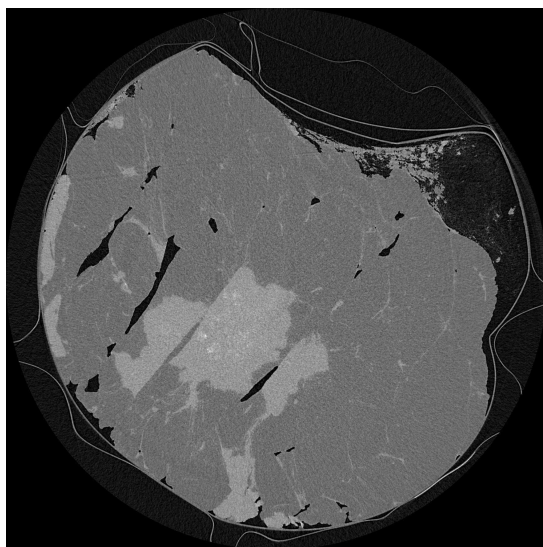


Fig. 11. Final reconstruction obtained subsequently applying the pre-processing procedure and the phase-retrieval.

## 4. Conclusions

In this work the effectiveness of the pre-processing procedure tailored for a multi-module single-photon-counting CdTe detector (PIXIRAD-8) was step-by-step discussed and demonstrated in the framework of a synchrotron radiation breast-CT experiment. The challenges concerning the presence of a dead space between adjacent modules, the time dependent gain variation due to charge trapping and crystal impurities and the non-optimal behavior of close-to-edge pixels have been specifically addressed. In particular, the dynamic flat fielding and ring removal procedures yielded better results if compared with standard techniques. In fact, the main advantage of the implemented algorithms is their ability to cope with pixels showing a time gain variation during the tomographic scan, which is a feature common to most of high-Z SPCDs while it is rarely encountered in conventional CT applications. Moreover, great care is taken in the filters optimization in order to preserve phase effects, which are of paramount importance in a synchrotron radiation based experiment. The effects of the pre-processing on the image quality were demonstrated using a breast specimen, which represents a challenging sample to be imaged due to the poor contrast between different tissues. In addition to the presented images, the pre-processing procedure has shown its effectiveness for a number of different test objects and biological samples, within a wide range of beam energies, photon fluences and detector thresholds (Contillo *et al.*, 2018; Brombal *et al.*, 2018). Moreover, an effective artifact suppression has been obtained for both phase-contrast and phase-retrieved images. For the sake of portability, the whole code of the pre-processing procedure is implemented in C language in order to be compiled and executed within all the operating systems and it is made available upon request to the corresponding author. It is the authors' belief that high-Z single-photon-counting detectors will be widely used in future CT applications, especially in medical imaging, due to their high-efficiency, low noise and

spectral performances: in this context, the pre-processing procedure presented in this work may represent a useful approach to be used in other applications.

Acknowledgements. The authors thank Prof F Zanconati MD and Dr Deborah Bonazza MD for providing and preparing the breast specimen. The SYRMA-3D project is supported by Istituto Nazionale di Fisica Nucleare (National Scientific Committee 5 for Technological and inter-disciplinary research) and Elettra-Sincrotrone Trieste S.C.p.A. Sandro Donato is partially supported by Consorzio per la Fisica Trieste.

## References

- Abrami, A., Arfelli, F., Barroso, R., Bergamaschi, A., Bille, F., Bregant, P., Brizzi, F., Casarin, K., Castelli, E., Chenda, V. *et al.* (2005). *Nuclear Instruments and Methods in Physics Research Section A: Accelerators, Spectrometers, Detectors and Associated Equipment*, **548**(1-2), 221–227.
- Astromskas, V., Gimenez, E. N., Lohstroh, A. & Tartoni, N. (2016). *IEEE Transactions on Nuclear Science*, **63**(1), 252–258.
- Ballabriga, R., Alozy, J., Campbell, M., Frojdh, E., Heijne, E., Koenig, T., Llopart, X., Marchal, J., Pennicard, D., Poikela, T. *et al.* (2016). *Journal of Instrumentation*, **11**(01), P01007.
- Bellazzini, R., Spandre, G., Brez, A., Minuti, M., Pinchera, M. & Mozzo, P. (2013). *Journal of Instrumentation*, **8**(02), C02028.
- Beltran, M., Paganin, D., Siu, K., Fouras, A., Hooper, S., Reser, D. & Kitchen, M. (2011). *Physics in medicine and biology*, **56**(23), 7353.
- Boin, M. & Haibel, A. (2006). *Optics Express*, **14**(25), 12071–12075.
- Brombal, L., Golosio, B., Arfelli, F., Bonazza, D., Contillo, A., Delogu, P., Donato, S., Mettivier, G., Oliva, P., Rigon, L. *et al.* (2018). In *Medical Imaging 2018: Physics of Medical Imaging*, vol. 10573, p. 1057320. International Society for Optics and Photonics.
- Brun, F., Delogu, P., Longo, R., Dreossi, D. & Rigon, L. (2017). *Measurement Science and Technology*, **29**(1), 014001.
- Burvall, A., Lundström, U., Takman, P. A., Larsson, D. H. & Hertz, H. M. (2011). *Optics Express*, **19**(11), 10359–10376.
- Contillo, A., Veronese, A., Brombal, L., Donato, S., Rigon, L., Taibi, A., Tromba, G., Longo, R. & Arfelli, F. (2018). *Radiology and Oncology*, *in press*.
- Delogu, P., Brombal, L., Di Trapani, V., Donato, S., Bottigli, U., Dreossi, D., Golosio, B., Oliva, P., Rigon, L. & Longo, R. (2017a). *Journal of Instrumentation*, **12**(11), C11014.
- Delogu, P., Golosio, B., Fedon, C., Arfelli, F., Bellazzini, R., Brez, A., Brun, F., Di Lillo, F., Dreossi, D., Mettivier, G. *et al.* (2017b). *Journal of Instrumentation*, **12**(01), C01016.
- Delogu, P., Oliva, P., Bellazzini, R., Brez, A., De Ruvo, P., Minuti, M., Pinchera, M., Spandre, G. & Vincenzi, A. (2016). *Journal of Instrumentation*, **11**(01), P01015.
- Fedon, C., Longo, F., Mettivier, G. & Longo, R. (2015). *Physics in Medicine & Biology*, **60**(16), N311.
- Knoll, G. F. (2010). *Radiation detection and measurement*. John Wiley & Sons.
- Longo, R. (2016). *Nuclear Instruments and Methods in Physics Research Section A: Accelerators, Spectrometers, Detectors and Associated Equipment*, **809**, 13–22.
- Longo, R., Arfelli, F., Bellazzini, R., Bottigli, U., Brez, A., Brun, F., Brunetti, A., Delogu, P., Di Lillo, F., Dreossi, D. *et al.* (2016). *Physics in medicine and biology*, **61**(4), 1634.
- Mettivier, G., Fedon, C., Di Lillo, F., Longo, R., Sarno, A., Tromba, G. & Russo, P. (2015). *Physics in Medicine & Biology*, **61**(2), 569.
- Mozzanica, A., Bergamaschi, A., Brueckner, M., Cartier, S., Dinapoli, R., Greiffenberg, D., Jungmann-Smith, J., Maliakal, D., Mezza, D., Ramilli, M. *et al.* (2016). *Journal of Instrumentation*, **11**(02), C02047.

- Münch, B., Trtik, P., Marone, F. & Stampanoni, M. (2009). *Optics express*, **17**(10), 8567–8591.
- Paganin, D., Mayo, S., Gureyev, T. E., Miller, P. R. & Wilkins, S. W. (2002). *Journal of Microscopy*, **206**(1), 33–40.
- Park, S. E., Kim, J. G., Hegazy, M., Cho, M. H. & Lee, S. Y. (2014). In *Proc. SPIE*, vol. 9033, p. 90335.
- Pennicard, D. & Graafsma, H. (2011). *Journal of Instrumentation*, **6**(06), P06007.
- Rivers, M., (1998). *Tutorial introduction to x-ray computed microtomography data processing*. [Http://www.mcs.anl.gov/research/projects/X-raycmt/rivers/tutorial.html](http://www.mcs.anl.gov/research/projects/X-raycmt/rivers/tutorial.html).
- Sarno, A., Mettievier, G., Golosio, B., Oliva, P., Spandre, G., Di Lillo, F., Fedon, C., Longo, R. & Russo, P. (2016). *Physica Medica*, **32**(5), 681–690.
- Taguchi, K. & Iwanczyk, J. S. (2013). *Medical physics*, **40**(10).
- Takahashi, T. & Watanabe, S. (2001). *IEEE Transactions on Nuclear Science*, **48**(4), 950–959.
- Van Nieuwenhove, V., De Beenhouwer, J., De Carlo, F., Mancini, L., Marone, F. & Sijbers, J. (2015). *Optics Express*, **23**(21), 27975–27989.
- Vedantham, S., Shrestha, S., Karellas, A., Shi, L., Gounis, M. J., Bellazzini, R., Spandre, G., Brez, A. & Minuti, M. (2016). *Medical physics*, **43**(5), 2118–2130.
- Vincenzi, A., De Ruvo, P., Delogu, P., Bellazzini, R., Brez, A., Minuti, M., Pinchera, M. & Spandre, G. (2015). *Journal of Instrumentation*, **10**(04), C04010.

---

### Synopsis

Supply a synopsis of the paper for inclusion in the Table of Contents.

---